Inorganic Chemistry

pubs.acs.org/IC

Article

Experimental Evidence of the Coexistence of Proper Magnetic and Structural Incommensurability on the $[CH_3NH_3][Ni(COOH)_3]$ Compound

Laura Cañadillas-Delgado,* Lidia Mazzuca, Oscar Fabelo,* Juan Rodríguez-Carvajal, and Vaclav Petricek

Cite This: https://dx.doi.org/10.1021/acs.inorgchem.0c01722

Read Online

ACCESS | Metrics & More | Article Recommendations | Supporting Information

ABSTRACT: The present work is dedicated to characterization of the structural phase transition and incommensurate magnetic structure of the $[CH_3NH_3][Ni(COOH)_3]$ (**1**) perovskite-like metal−organic compound. The structural and magnetic characterization has been performed through variable-temperature single-crystal and powder neutron diffraction. Compound **1** crystallizes in the orthorhombic *Pnma* space group at room temperature. Below 84 K, a new phase has been observed. The occurrence of new reflections, which can be indexed with a wavevector along the *c* axis [$\mathbf{q} = 0.1426(2)c^*$], suggests the occurrence of an incommensurately modulated crystal structure. The structure was determined using the superspace group formalism on the $Pnma(00\gamma)0s0$ space group. This incommensurate phase remains unchanged with a decrease of the temperature up to the base temperature (ca. 2 K). Moreover, the magnetic susceptibility data, collected under zero-field-cooled and field-cooled conditions at different applied magnetic fields, show that compound **1** exhibits antiferromagnetic behavior below 34 K. In the current paper, we have confirmed that compound **1** presents the coexistence of nuclear and proper magnetic incommensurability below T_N.

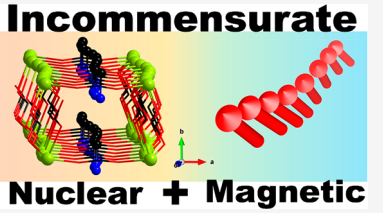

INTRODUCTION

The capability of the coordination polymers to combine several physical properties within the same framework has attracted vast interest in recent years.[1] One of the main features that metal−organic compounds can exhibit is magnetism, and the combination with other physical properties makes these systems multifunctional. Investigation of the magnetostructural correlations of these materials, aimed at understanding the chemical and structural factors that govern the exchange coupling between the paramagnetic centers, has become the subject of intense research because of their hybrid characteristics. These features are provided by a mixture of metal cations and organic ligands, which opens innumerable possibilities for the conception of new smart materials.[2] Moreover, these compounds have been proven to be good hosts for unique magnetic states, which are best understood using neutron diffraction.[3] Many studies have revealed carboxylate ligands as good linkers in the creation of secondary building units on coordination polymers and as good mediators of magnetic interactions.[4]

When the exchange interactions between magnetic ions are strong enough to overcome other effects such as thermal disorder, a long-range magnetically ordered state can be established. The coupling between magnetic moments is a quantum-mechanical phenomenon that, within a crystallographic network, may give rise to a magnetically ordered state.

Néel was the first to suggest that some substances, in which the magnetic susceptibility diminishes below a certain temperature, may contain antiparallel alignment of elemental magnetic moments.[5] Moreover, Néel proposed a new kind of ferromagnetism, including the concept of sublattices containing antiparallel moments.[6] The noncompensation (different magnitude of magnetic moments) of the two antiferrmagnetic coupled sublattices gives rise to a global ferromagnetic signal. This new magnetic order is called ferrimagnetic. In a ferrimagnet, the spins oppose each other; however, the opposing moments are unequal, so there is a spontaneous magnetization. The hypothesis of Néel was confirmed by the neutron diffraction experiment carried out by Shull et al.[7]

In the following years, many surprising magnetic structures were determined, i.e., noncollinear magnetic structures with a triangular configuration or the case of a weak ferromagnet due to a canted antiferromagnet, where the spins are tilted by a small angle about their principal axis.[8] To interpret the increasingly complex diffraction results, new concepts such as the *propagation vector* or *magnetic symmetry* of a magnetic structure were introduced.[9] These tools were essential to describing a new kind of magnetic structure that may not be described using the concept of "magnetic unit cell" in contraposition to the "chemical unit cell" (or nuclear/structural unit cell). The periodicity of a magnetic structure

Received: June 15, 2020

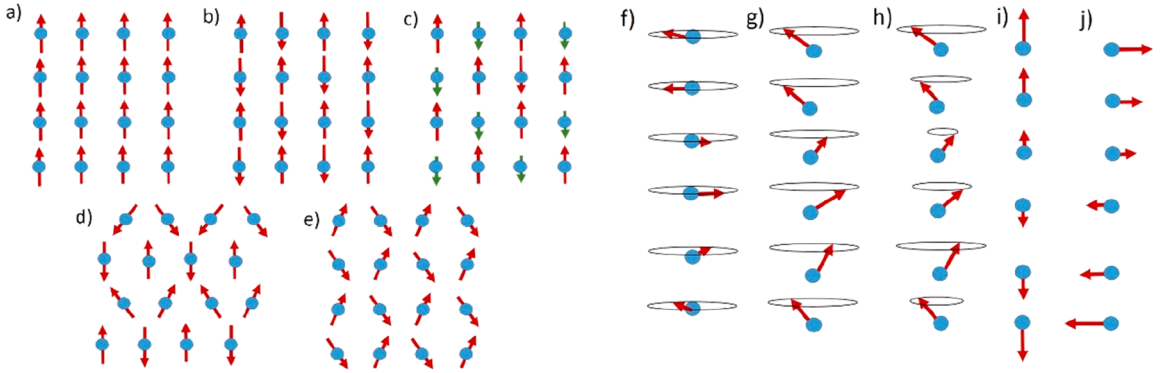

Figure 1. Schematic view of different simple types of atomic magnetic ordering. Magnetic structures: (a) ferromagnetic; (b) antiferromagnetic; (c) ferrimagnetic; (d) triangular; (e) weak ferromagnetic (spin-canting); (f) simple spiral; (g) ferromagnetic spiral; (h) complex spiral; (i) longitudinal spin wave; (j) traversal spin wave.

could be related to that of a "crystallographic" structure (paramagnetic structure). In the case of a nonmodulated crystal structure, if the magnetic cell is equal to or an integer multiple of the crystallographic unit cell, we say that the magnetic structure is commensurate, but if this is not the case, the magnetic structure should be considered to be incommensurate. Two independent groups led by Yoshimori and Villain from Japan and France, respectively, gave the theoretical foundation for understanding the case of helical structures.[10] These studies were confirmed by Herpin et al. on a $MnAu_2$ alloy.[11] Similar results were presented simultaneously by Koehler,[12] with this work being the first reported example of an incommensurate magnetic structure.

A magnetic structure can be defined in terms of magnetic modes.[13] These magnetic modes are classified in two main groups. The first group includes modes that modify the magnetic moments of the metal atoms in such a way that a periodic magnetic structure is reproduced. The second one contains modes that modulate the magnetic moments of the atoms depending on its position defined by a phase factor, t, named the incommensurate parameter.[14] In the case that a compound presents a nuclear incommensurate structure and long-range magnetic order, its magnetic structure is described as an incommensurate magnetic structure. Moreover, two types of incommensurability can be defined depending on the magnetic modes that are active. Incommensurate magnetic structures that only present magnetic modes in the first group can be described as "improper" because modulation of the magnetic structure comes from the incommensurable character of the nuclear structure. In other words, if the nuclear structure becomes periodic, the magnetic incommensurability will disappear. Incommensurate magnetic structures that present modes from the second group can be defined as "proper" because modulation of the magnetic moments depending on the incommensurate parameter, t, exists. In this case, magnetic incommensurability remains even if structural incommensurability is not present.

Nowadays, quite complex magnetic structures are known[15] (Figure 1), from complex cycloidal structures to skyrmions, and a detailed database including most of the reported magnetic structures can be consulted on MAGNDATA.[16] However, up to now there is no experimental evidence of the occurrence of structural and proper magnetic incommensurability on a single material. An example with structural and improper magnetic incommensurability was shown in the $BaMnF_4$ compound.[17] This compound presents a structural phase transition below T < 250 K with a wavevector of $\mathbf{k}$ = (0.392, $^1/_2$, $^1/_2$), while the ordered magnetic structure is described with a $\mathbf{k}$ = (0, $^1/_2$, $^1/_2$) commensurate propagation vector. The title compound develops long-range magnetic order below 34 K.[18] Moreover, the structural incommensurability shown by a Co-based isomorphous compound[19] suggests that the reported Ni-based compound can present the coexistence of proper magnetic and structural incommensurability.

In this paper, we present the structural and magnetic characterization of the $[CH_3NH_3][Ni(COOH)_3]$ (**1**) perovskite-like metal−organic compound. A combination of single-crystal and powder neutron diffraction has been used to accurately determine the sequence of phase transitions that lead to the coexistence of structural and magnetic incommensurability below T_N.

EXPERIMENTAL DETAILS

Sample Preparation. The synthetic route to obtain the $[CH_3NH_3][Ni(COOH)_3]$ (**1**) compound is equivalent to that of the previously reported $[CH_3NH_3][Co(COOH)_3]$ in ref 19. However, $NiCl_2{\cdot}6H_2O$ (3 mL, 0.33 M) was used instead of $CoCl_2{\cdot}6H_2O$. This synthesis allowed us to obtain prismatic green crystals of **1** suitable for single-crystal diffraction, with a yield of about 71%. The crystals were filtered, washed with ethanol (10 mL), and dried at room temperature (RT). FT-IR (cm^{-1}): ν(N−H) 3088(sh), $\nu_{s/as}$(N−H) 2763(w), δ_{as}(N−H) 1644(sh), $\nu(CH_3)$ 2857(w), 1458(w), 1420(w), ν_{as}(OCO) 1573(s), ν_s(OCO) 1351(s), δ_{as}(OCO) 1379(w), δ_s(OCO) 793(s), ν(C−N) 968(w).

Powder Neutron Diffraction (NPD) Measurements and Refinement Details. We performed NPD experiments on the high-intensity diffractometer D1B at the ILL (Grenoble, France) using a pyrolytic graphite monochromator, providing neutrons with a wavelength of λ = 2.521 Å. The sample (ca. 1 g) was placed in a ⌀ 6 mm cylindrical vanadium can inside a variable-temperature environment (orange cryostat). The diffraction patterns were recorded at 40 and 2 K, above and below the magnetic order temperature, respectively. Additionally, in order to obtain the global temperature-dependent diffraction pattern of the sample, we collected a thermodiffractogram in the 2−300 K range. Crystal structure refinements and magnetic structure calculations were carried out using the *FullProf Suite*[20] and *JANA2006*[21] programs.

Single-Crystal Neutron Laue Diffraction Measurements. Temperature evolution of the reciprocal space was surveyed through single-crystal neutron Laue diffraction on the multiple CCD diffractometer CYCLOPS (Cylindrical CCD Laue Octagonal Photo Scintillator) at the ILL (Grenoble, France).[22] The selected crystal, with dimensions of 1 × 1 × 0.7 mm^3, was mounted onto a vanadium pin and placed on a standard orange cryostat. The advantage of the

https://dx.doi.org/10.1021/acs.inorgchem.0c01722
Inorg. Chem. XXXX, XXX, XXX−XXX

CYCLOPS instrument is that we can perform a fast exploration of the reciprocal space as a function of an external parameter, like temperature. We recorded several diffraction patterns in the temperature range from 240 to 2 K. In order to center the sample on the neutron beam, we performed several scans in the *XYZ* directions until maximization of the intensity of some strong reflections was achieved. After that, we selected a specific orientation, and the temperature evolution was measured. We programmed a ramp of 0.2 K min^{-1} and collected each Laue diffraction pattern for 15 min, which made a difference of temperature of 3 K. These measurements showed the occurrence of a structural phase transition at ca. 84 K. Graphical visualization of the Laue patterns was performed with the *ESMERALDA* software developed at the ILL (Figure S1).[23]

Single-Crystal Neutron Diffraction Measurements. The same crystal that was used for neutron Laue diffraction measurements was installed on the self-dedicated low-temperature displex device on the monochromatic diffractometer D19 at the ILL (Grenoble, France). The wavelength used was 1.4547(1) Å for RT and 1.45376(10) Å for 40(1) and 5(1) K data collection, provided by a flat Cu monochromator using the 220 reflection, at a $2\theta_M = 69.91°$ takeoff angle. The wavelengths used were selected based on the instrumental resolution and data completeness and to avoid overlapping of neighboring reflections in the incommensurate phases. The crystal was cooled to 40(1) and 5(1) K with a 2 K min^{-1} cooling rate. The data acquisition strategy consisted of ω scans [10 at RT, 33 at 40(1) K, and 29 at 5(1) K] at different χ and φ positions with constant steps of 0.07°. In order to avoid collisions with the sample environment, these ω scans covered either 79° or 64° depending on the χ angle.[24]

For data collection, we used the Multi-Detector Acquisition Data Software (*MAD*) from the ILL. The *PFIND* and *DIRAX*[25] programs were used to determine the unit cell, and we processed the raw data using the new D19 suite of programs *Int3D* for the RT measurements and the *RETREAT* program for the incommensurate cases at 40(1) and 5(1) K. The refinements of the unit cell and offsets were performed with the *RAFD19* program.[26]

Possible wavevectors were calculated using the *DIRAX* program.[25] After that, each data set collected at a single temperature was indexed with a single wavevector in the form $\mathbf{q} = \gamma c^*$. This indexed wavevector was used to obtain a supercell. All reflections, main and satellites, were successfully integrated with this supercell. We used the new D19 software *SATELLITE* for decomposition into the main and satellite reflections, following the superspace formalism. Below 84 K, second-order satellites were observed. The *D19ABS* program[27] was used to perform the absorption correction, taking into account the experimental environment at each temperature.

Single-Crystal Structural and Magnetic Determination and Refinement Details. For structure refinement of the RT phase (parent orthorhombic phase), we used full matrix least-squares refinement on $|F^2|$ using *SHELXL*,[28] as implemented in the *WINGX* program. For the low-temperature data, the crystal structure was solved using the *SUPERFLIP* program, using a charge-flipping algorithm.[29] This program was used to localize the non-H atoms, while the positions of the H atoms were determined using the difference Fourier map in further refinement cycles. The incommensurate phases, magnetic and nuclear, from data at 40(1) and 5(1) K were refined using the superspace formalism, as implemented in the *JANA2006/JANA2020* program,[21] which for the moment is the only available program that can handle this approach. From analysis of the (3 + 1)D Fourier density maps, a strong displacive character close to harmonicity for both the framework and counterion could be appreciated. Therefore, to model the incommensurability, we included the displacement parameters of the different atoms in the refinement. Furthermore, neutron data allowed us to refine all atoms with anisotropic displacement parameters (ADPs). The magnetic **k** vector was determined to be (0, 0, 0), considering an incommensurate structure (nuclear) with the wavevector $\mathbf{q} = 0.1426(2)c^*$. The ratio between the main and satellite reflections is 0.26 for both the 40(1) and 5(1) K data sets, and the number of refined parameters are 220 and 226, respectively. A summary of the crystallographic and experimental data is given in Table 1.

Table 1. Crystallographic and Experimental Data of Compound 1, Measured on the Single-Crystal Neutron Diffractometer D19 at RT, 40(1) K, and 5(1) K

	$C_4H_9NiNO_6$	$C_4H_9NiNO_6$	$C_4H_9NiNO_6$
M	225.8	225.8	225.8
(super)space group	*Pnma*	*Pnma*(00γ)0s0	*Pn′ma′*(00γ)0s0
T, K	300(1)	40(1)	5(1)
a, Å	8.2969(4)	8.1801(4)	8.1724(3)
b, Å	11.5970(8)	11.5419(10)	11.5374(6)
c, Å	8.0461(4)	8.0976(5)	8.0925(3)
V, Å^3	774.19(8)	764.53(9)	763.03(6)
Z	4	4	4
modulation vector		$\mathbf{q} = 0.1426c^*$	$\mathbf{q} = 0.1426c^*$
ρ_{calc}, mg m^{-3}	1.937	1.9618	1.9656
λ, Å	1.4547(1)	1.45376(10)	1.45376(10)
μ, mm^{-1}	0.231	0.231	0.231
R_1, $I > 2\sigma(I)$ (all)	0.0336 (0.0382)	0.0628 (0.0906)	0.0778 (0.1119)
wR_2, $I > 2\sigma(I)$ (all)	0.0662 (0.0695)	0.0796 (0.0819)	0.1664 (0.1775)
abs corrn	numerical	numerical	numerical
no. of indep reflns	704	3371	3789
no. of main reflns		695	787
no. of first-order satellite reflns		1258	1494
no. of second-order satellite reflns		1418	1508

A graphical representation of all phases was carried out using the *DIAMOND* program, version 4.4.0,[30] and *VESTA* program, version 3.4.6.[31]

RESULTS AND DISCUSSION

Crystal Structure at RT. Although determination of the crystal structure of **1** at RT is not the main purpose of this work, a brief description based on the single-crystal diffraction data will be given in this section. The location and refinement of light atoms of the methylammonium counterions, which could not be accurately located using X-ray diffraction, will be added hereafter.

The crystal structure of compound **1** in the parent phase (RT) was previously described in the orthorhombic *Pnma* space group.[18] The crystal structure can be depicted as a 3D $[Ni(HCOO)_3]^-$ anionic framework, where the crystallographically independent Ni(II) ion is located in an inversion center and is 6-coordinated in an nearly ideal NiO_6 octahedron. This framework can be defined also as a $4^{12}\cdot6^3$ CPU perovskite-like topology in Schläfli notation. The classic perovskite structures are described as ABO_3 3D nets. The BO_3 net of the perovskite structure can be seen in our case for the Ni(II) atoms (B site) surrounded by formate ligands. The 3D network is built up by the metal centers connected between them through formate ligands in an anti−anti conformation. A methylammonium counterion sits on the cavities of the framework occupying the A sites of the classic perovskite

https://dx.doi.org/10.1021/acs.inorgchem.0c01722
Inorg. Chem. XXXX, XXX, XXX−XXX

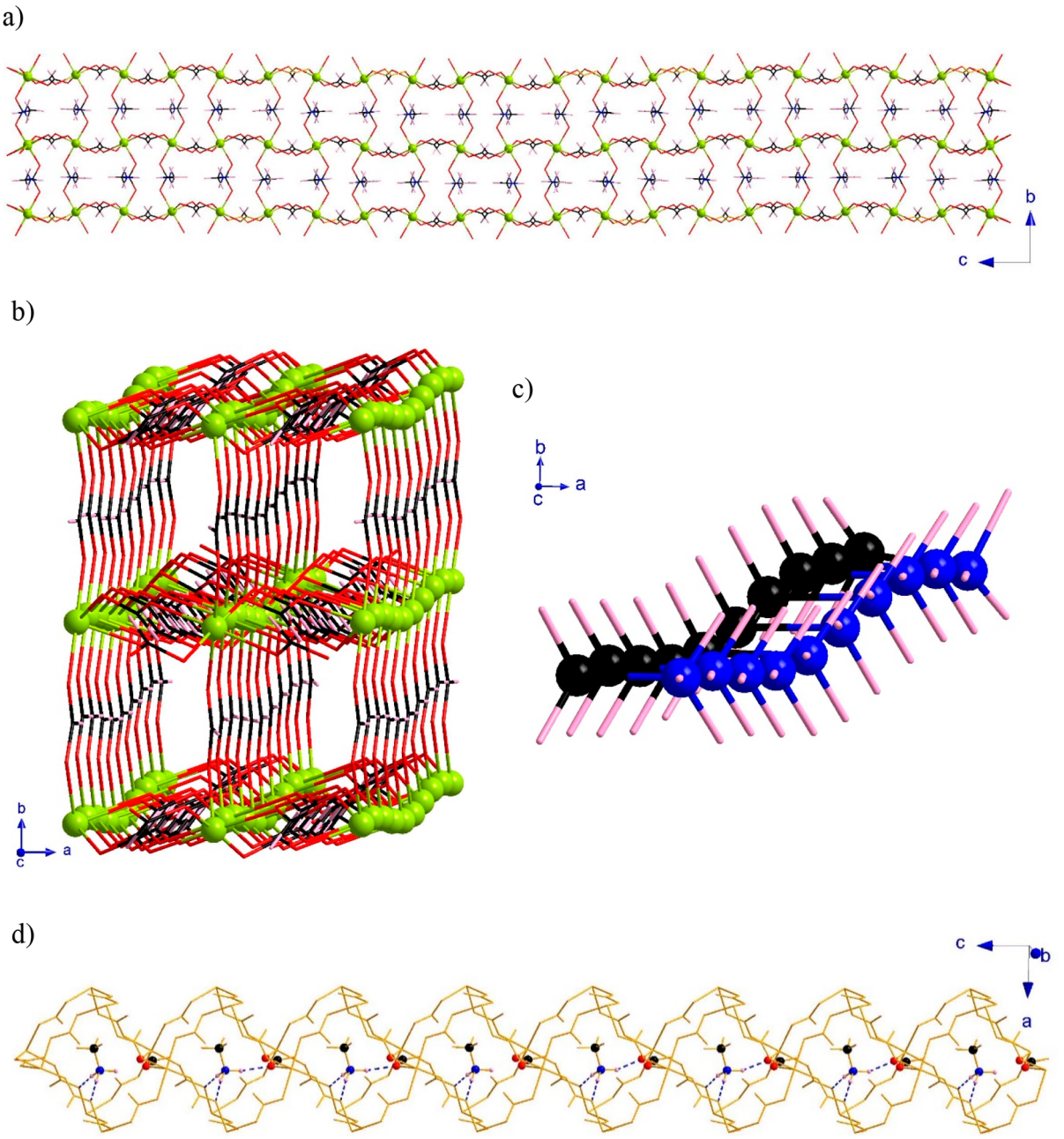

Figure 2. (a) View of a fragment along the *a* axis of the structure of **1**, obtained using single-crystal neutron diffraction at 40(1) K. Representations of the (b) 3D $Ni(COOH)^-$ network and (c) methylammonium counterions, where modulation of the atoms along the *c* axis with displacement mainly along the *b* axis could be appreciated. The Ni, C, O, N, and H atoms are represented as green, black, red, blue, and pink colors, respectively. (d) Representation of the possible hydrogen bonds involving the counterion and one of the formate ligands. The flip-flop behavior of the hydrogen bond along the *c* axis is highlighted using discontinuous blue lines. The graphical representations were accomplished by taking into account a supercell (10 times the average structure along the *c* axis) to include a full period.

model. The empty volume of the cavities is ca. 197 $Å^3$. Therefore, the methylammonium counterions have enough space to librate within the cavities. However, the $[CH_3NH_3]^+$ counterion is weakly anchored to the anionic framework, mainly involving van der Waals and hydrogen bond interactions. The refined model suggests that the three H atoms of the CH_3 group in the methylammonium molecule are equally disordered in two different positions. This structural disorder was previously observed in the Co-based compound at RT. With the current data, we cannot distinguish between a dynamic or static disorder. Moreover, it deserves to be noted that these H atoms do not establish any hydrogen bonds. In contrast, two of the three H atoms of the NH_3 group of the counterion are involved in hydrogen bonds. The role of the nonbonded H atom in the later phase transition at lower temperatures will be discussed in the following section.

At RT, the Ni(II)-based crystal structure is reminiscent of the previously reported Co(II)-based compound.[32,33] The disordered model on the counterion is equivalent; however, below RT, the series of phase transitions described on the Co(II)-based compound drastically differs from those reported here for the Ni(II)-based compound.

https://dx.doi.org/10.1021/acs.inorgchem.0c01722
Inorg. Chem. XXXX, XXX, XXX−XXX

Incommensurate Structure. Hereafter, we briefly describe the sequence of structural phase transitions previously studied on the Co(II) compound. The Co(II)-based compound presents three distinguishable phase transitions. The first one was at 128 K from the *Pnma* space group to the incommensurate $Pnma(00\gamma)0s0$ space group with $\mathbf{q} = 0.143c^*$. A second phase transition was below 96 K, maintaining structural incommensurability, with a significant change on the incommensurate wavevector from $\mathbf{q} = 0.143c^*$ to $\mathbf{q} = 0.1247c^*$. Moreover, at 78 K, the Co(II) compound suffered a third phase transition to a monoclinic phase, described on the $P2_1/n$ space group. Structural analysis suggests that the variaton along t on the hydrogen-bond interactions, in the incommensurate phase, promotes the phase transition between the two incommensurate phases.

In contrast to the Co-based compound, compound **1** shows a single phase transition below 84 K. A survey of the temperature of single-crystal neutron diffraction reveals that no further phase transition occurs. The nickel compound crystallizes in the $Pnma(00\gamma)0s0$ space group below 84 K, maintaining the same wave vector $\mathbf{q} = 0.1426(2)c^*$, which gives an almost 7-fold increase along the c axis. According to the determined superspace group, the average structure is described using the symmetry operators of the *Pnma* space group. The position of each independent atom in the average structure is modified by the application of a modulation function that exhibits sinusoidal behavior, with the amplitudes of the displacive modulation mainly over the b axis with a small component in the a axis for some atoms (Figures 2 and S2). Table 2 shows a summary of the refined displacement amplitudes for Ni(II) and the C and N atoms of the $[CH_3NH_3]^-$ counterion, as representative of the framework and guest molecule, respectively. These displacement amplitudes on compound **1** are slightly smaller than those of the previously reported Co(II) compound.[19]

Table 2. Displacement Amplitudes from the Cosine and Sine Terms of the First-Order Harmonics in the Fourier Series, Corresponding to the Ni Atom and the N and C Atoms from the $[CH_3NH_3]^-$ Counterion at 40(1) K[a]

	x	y	z
Ni sin	−0.00272(14)	0.02274(11)	0.00034(15)
N1 sin	0	0.02132(13)	0
N1 cos	0	0.00627(13)	0
C3 sin	0	0.02126(18)	0
C3 cos	0	0.00109(18)	0

[a]Note that the amplitude displacement from the cosine term of the Ni atom is zero.

Like on the Co(II) compound, in the case of the NiO_6 octahedron, the modulation amplitudes along the a, b, and c axes are allowed by symmetry, implying small structural tilts or distortions. However, the distortions along the a and c axes are notably smaller than those along the b axis, with the latter being mainly responsible for the observed modulation.

The hydrogen-bonded network established between the $[CH_3NH_3]^-$ counterion and the O atoms of the carboxylate ligand changes along the direction of modulation. The H atoms of the CH_3 group do not establish any hydrogen bond. However, two of the three H atoms connected to the N atom of the counterion clearly set hydrogen bonds with the nearest O atoms of two formate groups, while the last H atom oscillates between two O atoms from the same formate ligand (Figures 2d and S3 and S4), giving rise to a "flip-flop" behavior. Table S1 shows the possible hydrogen bonds defined along the incommensurate structure in terms of the t parameter (with t varying from 0.0 to 1.0 with steps of 0.1).

The Co-based compound undergoes a phase transition to a monoclinic structure at 78 K. However, nonbreaking of symmetry from an orthorhombic superspace group to monoclinic has been observed on the Ni-based compound. Therefore, the combination of structural incommensurability, together with the occurrence of long-range magnetic order, can lead to an unprecedented magnetic structure. A detailed discussion of the experimental data below T_N will be described in the following section.

Magnetic Structure. After crystal structure determination at 40(1) K, NPD on a D1B diffractometer, together with single-crystal measurements on a D19 instrument, was performed below the order temperature (ca. 34 K) to determine the magnetic structure of compound **1**.

NPD. Temperature evolution of compound **1** in the range from 40 to 300 K shows a slight shift of the reflections due to thermal expansion (Figure 3, left). It should be noted that, because of the high quantity of H atoms in compound **1** and the consequent incoherent scattering, structural incommensurability at low temperature is not visible with NPD. Moreover,

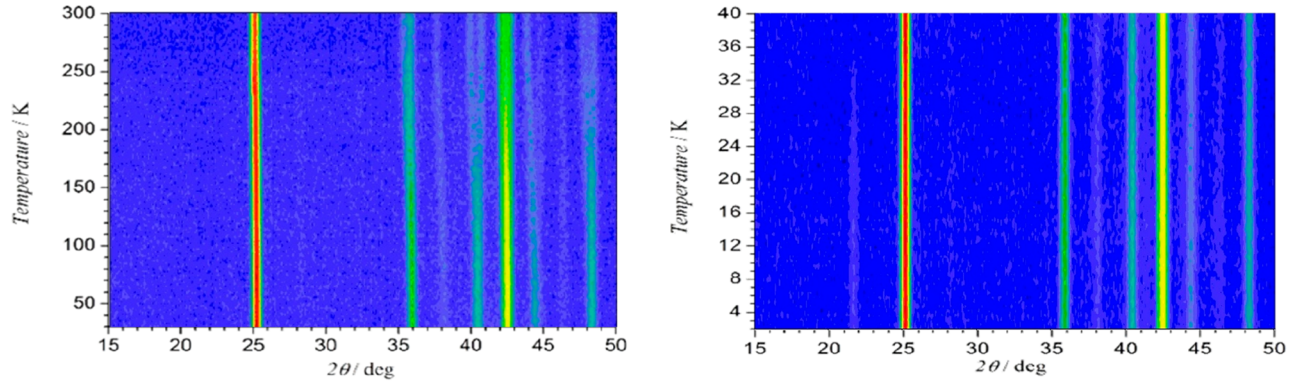

Figure 3. (left) Mesh plot of compound **1**, where the intensities are represented in the logarithmic scale, of the powder neutron thermodiffractogram in the temperature range of 40−300 K. (right) Thermodiffractogram in the temperature range of 2−40 K. Below 34 K, the presence of new reflections and the increase of the intensity on the top of the nuclear reflections suggest long-range magnetic order, in agreement with the reported T_N of this compound.

https://dx.doi.org/10.1021/acs.inorgchem.0c01722
Inorg. Chem. XXXX, XXX, XXX−XXX

there is no sign of a structural phase transition; therefore, the occurrence of a monoclinic phase at low temperature, like the Co(II) compound, can be discarded.

In the range from 40 to 2 K, the thermodiffractogram shows the occurrence of new reflections (Figure 3, right). The increase of the intensity of these reflections occurs around 34 K, in good agreement with the magnetometry measurements, and therefore these reflections should have magnetic character.[18] The indexing of these magnetic reflections was carried out using the K-search program, giving rise to the propagation vector **k** = (0, 0, 0). These new reflections at ca. 22° can correspond to the structurally forbidden (1 1 0) or to the allowed (0 1 1) in the *Pnma* space group, which are almost overlapped because of the instrument resolution. The difference patterns, between the ordered and paramagnetic states, have been used to refine the possible magnetic structure in the maximal space groups *Pnma′*, *Pnm′a′*, *Pn′m′a*, and *Pn′ma′*. However, from the difference pattern, only one clear set of magnetic reflections are observed (Figure S5). The low number of magnetic observations is, in part, related to the high incoherent background due to H atoms and the spin value of the Ni(II) ion at high spin, which is $s = 1$, and therefore it has only two unpaired electrons.

The susceptibility measurements of compound **1** show that magnetic interactions among the metal centers have dominant antiferromagnetic character, with the occurrence of a weak ferromagnetic signal below T_N, probably due to spin canting or the noncompensation of the magnetic moments.[18] Therefore, those maximal space groups, which preclude by symmetry the occurrence of a ferromagnetic component, can be discarded as a possible solution. In this particular case, the only one that does not allow a ferromagnetic component is *Pnma*; moreover, the refinement in this group is very bad. The *Pnm′a′* space group does not fit the experimental data; consequently, it was discarded. The refinement in the *Pn′m′a* magnetic group gives a magnetic structure with magnetic moments along the *b* axis and antiferromagnetically coupled with all of the adjacent neighbors. Although this model permits a ferromagnetic component along the *c* axis, our data do not permit us to refine this component. The refined values of the magnetic moments using this model give rise to a value of 2.03(5) μ_B with a R_f factor of ca. 2%. However, from the single-crystal magnetometry measurements presented by Pato-Doldán et al., we know that the easy axis in this compound is established along the *b* axis.[18] That means that the ferromagnetic component should be along this axis, due to spin canting. Therefore, we discarded this space group even though the data refinement was in agreement with the model.

The fit carried out using the *Pn′ma′* magnetic group gives rise to a magnetic structure, where the magnetic moments are along the *c* axis, and as in the previous case, each magnetic moment is antiferromagnetically coupled with the adjacent ones (Figure 4). This magnetic space group allows a ferromagnetic component along the *b* axis, which is compatible with the previous magnetometry measurements. However, because of the low number of observations, this component cannot be refined and has been fixed to zero. The refined values of the magnetic moments using this model give rise to a value of 2.04(5) μ_B with a R_f factor of ca. 2%.

Although the description of the magnetic structure along this section has been done using Shubnikov space groups, after the results obtained from single-crystal neutron diffraction below T_N, an alternative refinement can be done using the superspace

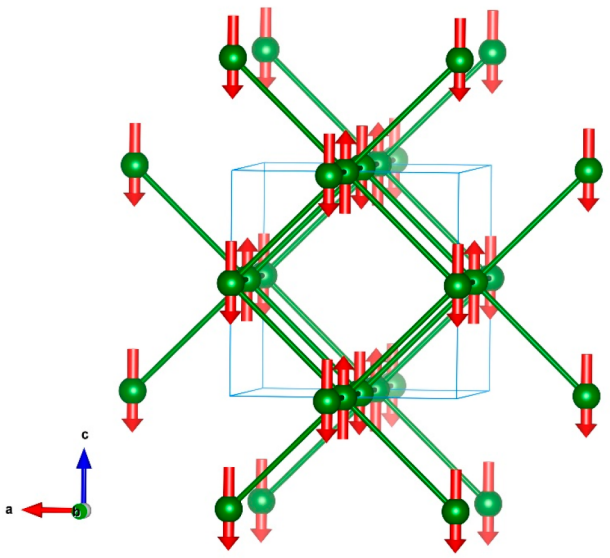

Figure 4. View of the magnetic structure refined in the *Pn′ma′* Shubnikov space group along the *b* axis, where only the magnetic sites are represented. The Ni atoms are displayed in green, and the magnetic moments are given as red arrows. The green bonds between Ni atoms are only a guide for the eye.

group formalism. A fit of the powder data using the model obtained from the single-crystal data with the superspace formalism is shown in Figure S6.

Single-Crystal Neutron Diffraction. Single-crystal neutron diffraction has been performed on the D19 instrument at 5(1) K. We have used the *ISODISTORT* suite[13] to evaluate the combination of displacive and magnetic distortions, in order to calculate the irreducible representations (*irreps*) to describe the full list of possible superspace magnetic groups. Calculation was done using two independent modulation vectors, one related to the structural distortion, **q** = 0.1426*c** and the second one related to the magnetic contribution, over the previously distorted structure and, therefore, incommensurate from the structural point of view. The magnetic contribution into the incommensurate phase can be described using the **k** = (0, 0, 0) propagation vector , which is compatible with the propagation vector obtained for the NPD experiment. So, **k** = (0, 0, 0) contributes to the nuclear incommensurate reflections, and the magnetic superspace group should be of type 3: it cannot contain the operator {1′|0001/2}. This fact involves that all of the magnetic signals are on top of the structural, main, or satellite reflections.

The choice of each particular *irrep* affects the symmetry of the atomic displacements (structural or magnetic). In this particular case, the combination of the different *irreps* gives rise to a list of 32 possible superspace magnetic groups (Table 3). However, the magnetometry results combined with the models obtained using the powder data, even if Shubnikov space groups were used, can help us to reduce the possible numbers of compatible superspace groups.

On the basis of NPD measurements, where the satellite reflections are not observed, the best magnetic model was refined on the Shubnikov space group *Pn′ma′*. However, on the basis of the single-crystal data on the paramagnetic phase [40(1) K], the structural model was refined using the superspace crystallographic group, *Pnma*(00γ)0*s*0. Our first attempt was to combine both models, giving rise to the

https://dx.doi.org/10.1021/acs.inorgchem.0c01722
Inorg. Chem. XXXX, XXX, XXX−XXX

Table 3. List of Possible Superspace Groups Compatible with the Distortion Modes Obtained from Considering k = (0, 0, 0) and q = 0.1426c* as Modulation Vectors for the Magnetic and Nuclear Distortions, Respectively

$Pnma(00\gamma)000$, origin = (0, 0, 0, 0)	$Pnma(00\gamma)0s0$, origin = (0, 0, 0, 0)
$Pmn2_1(00\gamma)000$, origin = ($-^1/_4$, $^1/_4$, 0, 0)	$Pmn2_1(00\gamma)s0s$, origin = ($-^1/_4$, $^1/_4$, 0, 0)
$Pn'm'a(00\gamma)000$, origin = (0, 0, 0, 0)	$Pn'm'a(00\gamma)0s0$, origin = (0, 0, 0, 0)
$Pm'n'2_1(00\gamma)000$, origin = ($-^1/_4$, $^1/_4$, 0, 0)	$Pm'n'2_1(00\gamma)s0s$, origin = ($-^1/_4$, $^1/_4$, 0, 0)
$Pnm'a'(00\gamma)000$, origin = (0, 0, 0, 0)	$Pnm'a'(00\gamma)0s0$, origin = (0, 0, 0, 0)
$Pm'n2_1'(00\gamma)000$, origin = ($-^1/_4$, $^1/_4$, 0, 0)	$Pm'n2_1'(00\gamma)s0s$, origin = ($-^1/_4$, $^1/_4$, 0, 0)
$Pn'ma'(00\gamma)000$, origin = (0, 0, 0, 0)	$Pn'ma'(00\gamma)0s0$, origin = (0, 0, 0, 0)
$Pmn'2_1'(00\gamma)000$, origin = ($-^1/_4$, $^1/_4$, 0, 0)	$Pmn'2_1'(00\gamma)s0s$, origin = ($-^1/_4$, $^1/_4$, 0, 0)
$Pnma(00\gamma)0s0$, origin = (0, 0, 0, $^3/_4$)	$Pnma(00\gamma)000$, origin = (0, 0, 0, $^3/_4$)
$Pmn2_1(00\gamma)s0s$, origin = ($-^1/_4$, $^1/_4$, 0, 0)	$Pmn2_1(00\gamma)000$, origin = ($-^1/_4$, $^1/_4$, 0, 0)
$Pn'm'a(00\gamma)0s0$, origin = (0, 0, 0, $^3/_4$)	$Pn'm'a(00\gamma)000$, origin = (0, 0, 0, $^3/_4$)
$Pm'n'2_1(00\gamma)s0s$, origin = ($-^1/_4$, $^1/_4$, 0, 0)	$Pm'n'2_1(00\gamma)000$, origin = ($-^1/_4$, $^1/_4$, 0, 0)
$Pnm'a'(00\gamma)0s0$, origin = (0, 0, 0, $^3/_4$)	$Pnm'a'(00\gamma)000$, origin = (0, 0, 0, $^3/_4$)
$Pm'n2_1'(00\gamma)s0s$, origin = ($-^1/_4$, $^1/_4$, 0, 0)	$Pm'n2_1'(00\gamma)000$, origin = ($-^1/_4$, $^1/_4$, 0, 0)
$Pn'ma'(00\gamma)0s0$, origin = (0, 0, 0, $^3/_4$)	$Pn'ma'(00\gamma)000$, origin = (0, 0, 0, $^3/_4$)
$Pmn'2_1'(00\gamma)s0s$, origin = ($-^1/_4$, $^1/_4$, 0, 0)	$Pmn'2_1'(00\gamma)000$, origin = ($-^1/_4$, $^1/_4$, 0, 0)

$Pn'ma'(00\gamma)0s0$ superspace group. It deserves to be noted that this superspace group is compatible with the macroscopic magnetometry measurements, where a noncompensated ferromagnetic signal was observed along the *b* axis.

Analysis of the symmetry of the $Pn'ma'(00\gamma)0s0$ superspace group shows that there are 12 free modes for the magnetic atoms, which are divided into displacive, magnetic, and strain modes. There are three strain modes, each one being a linear combination of the six strain components. The strain modes in this particular case can be omitted from the discussion because the unit-cell variations have been considered during the indexing procedure, and therefore these modes are not used during the data refinement. The three displacive modes are responsible for structural modulation of the Ni atoms, while the six remaining modes are pure magnetic [the *x*, *y*, and *z* components of the homogeneous moment, corresponding to **k** = (0, 0, 0), and three sinusoidal modulations with amplitudes along *x*, *y*, and *z*] and allow one to obtain the relative orientation and magnitude of the magnetic moments. It should be noted that only the three "sinusoidal" modes contribute to the "magnetic incommensurability", while the other three modes keep the translational symmetry of the magnetic moments along the *c* axis. Considering the complete structure, 226 parameters were refined. Up to 6 parameters were used to refine the magnetic structure and 220 to refine the structural modulation using up to second-harmonic modulation waves.

In our case, the best-fit results agree with our guess in the $Pn'ma'(00\gamma)0s0$ with an origin = (0, 0, 0, 0) magnetic superspace group. During the refinement, the value of the magnetic moment has been restricted to avoid values without physical meaning. The obtained value for the Ni(II) magnetic moment is, on average, 2.14(9) μ_B, and a small modulation in the magnetic moment modulus is observed; however, the variation (2.14−2.15 μ_B) is within the error bar of our refinement. This result corresponds to the NPD results using the Shubnikov space group, and it is realistic for a high-spin *s* = 1 Ni ion. The magnetic moments are pointing principally along the *c* axis, forming chains oriented ferromagnetically along this direction and antiferromagnetically coupled with the adjacent ones in the *a* and *b* directions. The magnetic moments are tilted along the *b* axis, resulting in a nonzero ferromagnetic component along this direction, in agreement with Pato-Doldán et al.[18] The direction of the magnetic moment is modulated by applying a modulation function that exhibits sinusoidal behavior. The main contribution to the magnetic modulation amplitude is along the *a* axis (Table 4). Because of symmetry constraints, only the cosine terms are allowed to be different from zero. Moreover, the component along the *b* axis can be fixed to zero because the component is smaller than the error bar. The amplitude of magnetic modulation along the *c* axis is almost 4 times weaker than that along the *a* axis. The application of these two modulation components produces a libration of the magnetic moment in the *ac* plane (Figure 5).

Table 4. Amplitude Displacements from the Cosine Terms of the First-Order Harmonics in the Fourier Series of Magnetic Moments of the Ni Atom[a]

	x	*y*	*z*
Ni cos	0.249(18)	0.02(6)[b]	−0.064(16)

[a]Note that the amplitude displacement from the sine term is zero because of the restrictions of the magnetic space group. [b]This component has been fixed to zero in the last cycle of refinement.

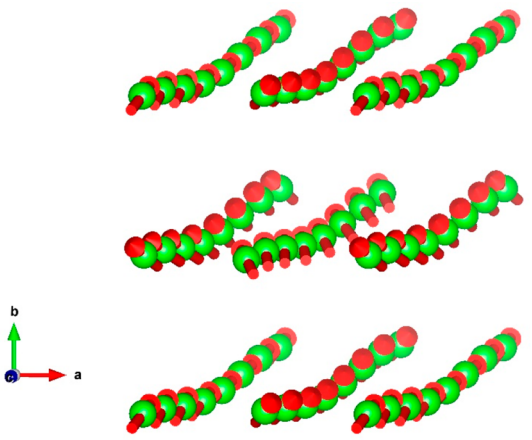

Figure 5. View of the refined magnetic moments of Ni(II) in the $Pn'ma'(00\gamma)0s0$ magnetic superspace group. For the sake of the clarity, only the Ni atoms are represented. In order to include at least a full period, the graphical representation was performed considering a supercell that is 10 times the average structure along the *c* axis. The Ni atoms are represented in green, and the magnetic moments are given as red arrows.

Although the application of magnetic modulation functions can be omitted, refining the system with Ni(II) $\text{cosine}_{(x,y,z)}$ components equal to zero, the final statistics indicators are worse than those if these components are included in the model. A comparison of the refinement of each model can be seen in Table S2. Moreover, the refinement using a superspace group allows us to refine the homogeneous ferromagnetic

https://dx.doi.org/10.1021/acs.inorgchem.0c01722
Inorg. Chem. XXXX, XXX, XXX−XXX

component along the b axis, giving a value of 0.55(9) μ_B. However, the refined value is notably higher than the value obtained by Pato-Doldán et al., using single-crystal magnetometry measurements (ca. 0.1 μ_B).[18] Although the refinement successfully converged, leaving free all of the parameters, if the magnetic component along the b axis is fixed to have the value obtained from the magnetometry results, there is not a significant change on the final statistics indicators, and therefore this parameter can be fixed.

The refined magnetic structure of the Ni(II) ion reminds one of that previously determined on the Co(II) compounds, solved on the $Pn'ma'$ Shubnikov space group. The magnetic structure of the Co-based compound corresponds to a weak ferromagnetic structure due to spin canting along the b axis. The Co(II) magnetic moments are oriented mainly along the c axis, forming chains oriented ferromagnetically along this direction and antiferromagnetically coupled with the adjacent ones along the a and b directions. The refined ferromagnetic component along the b axis was 0.68(12) μ_B, a value similar to that obtained on the Ni compound [0.55(9) μ_B].

CONCLUSION

Compound **1** crystallizes in the *Pnma* orthorhombic space group at RT. At this temperature, the title compound is isomorphous to the Co(II) analogous. Upon cooling, compound **1** presents a single phase transition to an incommensurate structure, which can be solved on the $Pnma(00\gamma)0s0$ superspace group. A similar periodic-to-incommensurate phase transition has already been observed on the Co(II)-based compound.[19] However, although both compounds at RT are isomorphous, their sequences of phase transitions are quite different. From a structural point of view, the origin of the incommensurate structure of both compounds should be the competition of the hydrogen bonds between the counterions and framework. Furthermore, they present similar wavevectors in the periodic-to-incommensurate phase transition. However, below this point, neither the structural nor magnetic behaviors of both compounds are comparable.

The unprecedented behavior of the Ni(II) compound, with an incommensurate structural phase up to the base temperature (ca. 2 K), allows the combination of structural incommensurability with long-range magnetic order. Determination of possible superspace groups compatible with the magnetic observations led to $Pn'ma'(00\gamma)0s0$ as the best-fit superspace group. The incommensurability observed on the Ni compound can be modeled including structural and magnetic modulations. The $Pn'ma'(00\gamma)0s0$ superspace group as the $Pn'ma'$ Shubnikov space group allows a ferromagnetic component along the b axis, which is in agreement with the preliminary magnetometry measurements.[18] From the magnetic point of view, the topology of the magnetic structure of the nickel compound is similar to that obtained for the cobalt compound. However, to reproduce the experimental data, magnetic modulations should be applied to the non-compensated antiferromagnetic structure. The magnetic modulations are acting mainly on the x component of the magnetic moment, and a much weaker contribution is applied on the z component of the magnetic moment. The combination of these two components allows each magnetic moment to be slightly shifted on the ac plane with respect to the magnetic moments of the adjacent metallic center along the c axis. The magnetic modulation amplitudes act perpendicularly to the main structural modulation amplitude, which produces the largest atomic shift along the b axis. The structural modulation on the Ni atom has a remarkable effect in the crystal structure, giving rise to a maximum displacement of 0.303(5) Å, a value that is notably larger than the variation on the bond distances on the framework or the counterion (Figure S7). It deserves to be noted that the maximum atomic displacement appears along the b axis in the H_6 atom, which is involved in the hydrogen bond with "flip-flop" behavior along the c axis.

The coexistence of structural modulation with long-range magnetic order below 34 K on compound **1** is a necessary but not sufficient requirement to obtain the coexistence of structural and proper magnetic incommensurability in a single phase. The application of displacive modes to the crystal structure produces necessarily the same displacement on the magnetic moments network, giving rise to an improper magnetic incommensurability because magnetic incommensurability is strongly coupled with structural incommensurability. However, for those cases where the magnetic moments network presents a modulation due to the occurrence of incommensurate magnetic modes, they can be described as a proper magnetic incommensurability, presenting a weak coupling with the structural features. The results presented on compound **1** show that it is a rare case where structural incommensurability and proper magnetic incommensurability coexist in a unique phase.

ASSOCIATED CONTENT

Supporting Information

The Supporting Information is available free of charge at https://pubs.acs.org/doi/10.1021/acs.inorgchem.0c01722.

> Temperature evolution of the neutron Laue patterns, representation of the refined modulation functions for the Ni atom obtained from the single-crystal neutron data refinement at 40(1) K, view of the asymmetric unit of the average structure at 40(1) K, modulation of the bond lengths between the third H atom of the NH_3 group of the methylammonium counterion and the closest O atom from formate ligand at 40(1) K, NPD patterns collected in the ordered and paramagnetic phases at 2 and 40 K, respectively, table of selected distances and angles involving the methylammonium counterion at 40(1) K, fit of the NPD pattern at 2 K using the superspace group formalism, comparison of the different refinements of the magnetic model, and graphical comparison of the modulation displacements for selected atoms along the b axis (PDF)

Accession Codes

CCDC 2010953−2010955 contain the supplementary crystallographic data for this paper. These data can be obtained free of charge via www.ccdc.cam.ac.uk/data_request/cif, or by emailing data_request@ccdc.cam.ac.uk, or by contacting The Cambridge Crystallographic Data Centre, 12 Union Road, Cambridge CB2 1EZ, UK; fax: +44 1223 336033.

AUTHOR INFORMATION

Corresponding Authors

Laura Cañadillas-Delgado − *Institut Laue Langevin (ILL), 38042 Grenoble Cedex 9, France;* orcid.org/0000-0001-8679-5008; Email: lcd@ill.fr

https://dx.doi.org/10.1021/acs.inorgchem.0c01722
Inorg. Chem. XXXX, XXX, XXX−XXX

Oscar Fabelo − *Institut Laue Langevin (ILL), 38042 Grenoble Cedex 9, France*; orcid.org/0000-0001-6452-8830; Email: fabelo@ill.fr

Authors

Lidia Mazzuca − *Institut Laue Langevin (ILL), 38042 Grenoble Cedex 9, France*

Juan Rodríguez-Carvajal − *Institut Laue Langevin (ILL), 38042 Grenoble Cedex 9, France*

Vaclav Petricek − *Institute of Physics, Academy of Sciences of the Czech Republic, 18040 Praha 8, Czech Republic*

Complete contact information is available at: https://pubs.acs.org/10.1021/acs.inorgchem.0c01722

Notes

The authors declare no competing financial interest.

■ ACKNOWLEDGMENTS

We are grateful to the ILL for the allocated neutron beam-time through Projects 5-41-947 and CRG-2369. We especially thank Dr. Nebil A. Katcho for providing the *Int3D* single-crystal integration software. The Czech Science Foundation through Project 18-10504S supports development of the *JANA* software.

■ REFERENCES

(1) (a) Zhu, Q. L.; Xu, Q. Metal-organic framework composites. *Chem. Soc. Rev.* **2014**, *43*, 5468−5512. (b) Cui, Y.; Li, B.; He, H.; Zhou, W.; Chen, B.; Qian, G. Metal-Organic Frameworks as Platforms for Functional Materials. *Acc. Chem. Res.* **2016**, *49*, 483−493. (c) Lin, Z.-J.; Lü, J.; Hong, M.; Cao, R. Metal-organic frameworks based on flexible ligands (FL-MOFs): structures and applications. *Chem. Soc. Rev.* **2014**, *43*, 5867−5895. (d) Liu, D.; Lu, K.; Poon, C.; Lin, W. Metal-Organic Frameworks as Sensory Materials and Imaging Agents. *Inorg. Chem.* **2014**, *53*, 1916−1924. (e) Li, B.; Wen, H.-M.; Cui, Y.; Zhou, W.; Qian, G.; Chen, B. Emerging Multifunctional Metal-Organic Framework Materials. *Adv. Mater.* **2016**, *28*, 8819−8860. (f) Liu, K.; Zhang, X.; Meng, X.; Shi, W.; Cheng, P.; Powell, A. K. Constraining the coordination geometries of lanthanide centers and magnetic building blocks in frameworks: a new strategy for molecular nanomagnets. *Chem. Soc. Rev.* **2016**, *45*, 2423−2439.

(2) (a) Coronado, E.; Mínguez Espallargas, G. Dynamic magnetic MOFs. *Chem. Soc. Rev.* **2013**, *42*, 1525−1539. (b) Luo, X.-L.; Yin, Z.; Zeng, M.-H.; Kurmoo, M. The construction, structures, and functions of pillared layer metal-organic frameworks. *Inorg. Chem. Front.* **2016**, *3*, 1208−1226. (c) Coronado, E. Molecular magnetism: from chemical design to spin control in molecules, materials and devices. *Nat. Rev. Mater.* **2020**, *5*, 87−104. (d) Verdaguer, M.; Gleizes, A. N. Magnetism: Molecules to Build Solids. *Eur. J. Inorg. Chem.* **2020**, *2020*, 723−731.

(3) For example, see: (a) Herren, F.; Fischer, P.; Ludi, A.; Haelg, W. Neutron diffraction study of Prussian Blue, $Fe_4[Fe(CN)_6]_3.xH_2O$. Location of water molecules and long-range magnetic order. *Inorg. Chem.* **1980**, *19* (4), 956−959. (b) Manson, J. L.; Huang, Q. Z.; Lynn, J. W.; Koo, H.-J.; Whangbo, M.-H.; Bateman, R.; Otsuka, T.; Wada, N.; Argyriou, D. N.; Miller, J. S. Long-Range Magnetic Order in $Mn[N(CN)_2]_2(pyz)\{pyz\}$pyrazine}. Susceptibility, Magnetization, Specific Heat, and Neutron Diffraction Measurements and Electronic Structure Calculations. *J. Am. Chem. Soc.* **2001**, *123*, 162−172. (c) Tustain, K.; Farrar, L.; Yao, W.; Lightfoot, P.; da Silva, I.; Telling, M. T. F.; Clark, L. Materialization of a Geometrically Frustrated Magnet in a Hybrid Coordination Framework: A Study of the Iron(II) Oxalate Fluoride Framework, $KFe(C_2O_4)F$. *Inorg. Chem.* **2019**, *58*, 11971−11977. (d) Saines, P. J.; Bristowe, N. C. Probing magnetic interactions in metal-organic frameworks and coordination polymers microscopically. *Dalton Trans.* **2018**, *47*, 13257−13280. (e) Bassey, E. N.; Paddison, J. A. M.; Keyzer, E. N.; Lee, J.; Manuel, P.; da Silva, I.; Dutton, S. E.; Grey, C. P.; Cliffe, M. J. Strengthening the Magnetic Interactions in Pseudobinary First-RowTransition Metal Thiocyanates, $M(NCS)_2$. *Inorg. Chem.* **2020**, *59*, 11627−11639.

(4) (a) Ma, P.; Hu, F.; Wang, J.; Niu, J. Carboxylate covalently modified polyoxometalates: From synthesis, structural diversity to applications. *Coord. Chem. Rev.* **2019**, *378*, 281−309. (b) Whitehead, G. F. S.; Ferrando-Soria, J.; Christie, L. G.; Chilton, N. F.; Timco, G. A.; Moro, F.; Winpenny, R. E. P. The acid test: the chemistry of carboxylic acid functionalised $\{Cr_7Ni\}$ rings. *Chem. Sci.* **2014**, *5*, 235−239. (c) Yue, Q.; Gao, E.-Q. Azide and carboxylate as simultaneous coupler for magnetic coordination polymers. *Coord. Chem. Rev.* **2019**, *382*, 1−31. (d) Wang, Z.; Hu, K.; Gao, S.; Kobayashi, H. Formate-based Magnetic Metal-Organic Frameworks Templated by Protonated Amines. *Adv. Mater.* **2010**, *22*, 1526−1533. (e) Wang, Z.; Zhang, B.; Inoue, K.; Fujiwara, H.; Otsuka, T.; Kobayashi, H.; Kurmoo, M. Occurrence of a Rare $4^9{\cdot}6^6$ Structural Topology, Chirality, and Weak Ferromagnetism in the $[NH_4][M^{II}(HCOO)_3]$ (M = Mn, Co, Ni) Frameworks. *Inorg. Chem.* **2007**, *46*, 437−445.

(5) (a) Néel, L. Propriétés magnétiques des ferrites; ferrimagnétisme et antiferromagnétisme. *Ann. Phys.* **1948**, *12*, 137−198. (b) Néel, L. Antiferromagnetism and Ferrimagnetism. *Proc. Phys. Soc., London, Sect. A* **1952**, *A65*, 869−885.

(6) Néel, L. Some New Results on Antiferromagnetism and Ferromagnetism. *Rev. Mod. Phys.* **1953**, *25*, 58−63.

(7) Shull, C. G.; Strauser, W. A.; Wollan, O. Neutron Diffraction by Paramagnetic and Antiferromagnetic Substances. *Phys. Rev.* **1951**, *83*, 333−345.

(8) (a) Moriya, T. Theory of Magnetism of NiF_2. *Phys. Rev.* **1960**, *117*, 635−647. (b) Dzyaloshinsky, I. A thermodynamic theory of "weak" ferromagnetism of antiferromagnetics. *J. Phys. Chem. Solids* **1958**, *4* (4), 241−255. (c) Bertaut, E. F. Configurations colineaires de spins dans les structures du type corindon. *Compt. Rend.* **1961**, 252−254.

(9) (a) Tavger, B. A.; Zaitsev, V. M. Magnetic Symmetry of Crystals. *J. Exptl. Theoret. Phys.* **1956**, *30*, 564−568. (b) Bertaut, E. F. Representation analysis of magnetic structures. *Acta Crystallogr., Sect. A: Cryst. Phys., Diffr., Theor. Gen. Crystallogr.* **1968**, *A24*, 217−231. (c) Bertaut, E. F. Magnetic Structure Analysis and Group Theory. *J. Phys. Colloques* **1971**, *32*, C1-462−C1-470.

(10) (a) Yoshimori, A. A New Type of Antiferromagnetic Structure in the Rutile Type Crystal. *J. Phys. Soc. Jpn.* **1959**, *14*, 807−821. (b) Villain, J. La structure des substances magnetiques. *J. Phys. Chem. Solids* **1959**, *11*, 303−309.

(11) (a) Herpin, A.; Meriel, P.; Villain, J. Antiferromagnétisme hélicoïdal. *J. Phys. Radium* **1960**, *21*, 67−67. (b) Herpin, A. Structures magnétiques nouvelles. *J. Phys. Radium* **1962**, *23*, 453−459.

(12) Koehler, W. C. Neutron Diffraction by Helical Spin Structures. *J. Appl. Phys.* **1961**, *32*, S20−S21.

(13) *ISODISTORT 6.3.5*: Campbell, B. J.; Stokes, H. T.; Tanner, D. E.; Hatch, D. M. ISODISPLACE: a web-based tool for exploring structural distortions. *J. Appl. Crystallogr.* **2006**, *39*, 607−614.

(14) Petříček, V.; Eigner, V.; Dušek, M.; Cejchan, A. Discontinuous modulation functions and their application for analysis of modulated structures with the computing system JANA2006. *Z. Kristallogr. - Cryst. Mater.* **2016**, *231* (5), 301−312.

(15) Rodriguez-Carvajal, J.; Villain, J. Magnetic structures. *C. R. Phys.* **2019**, *20*, 770−802.

(16) (a) Gallego, S. V.; Perez-Mato, J. M.; Elcoro, L.; Tasci, E. S.; Hanson, R. M.; Momma, K.; Aroyo, M. I.; Madariaga, G. MAGNDATA: towards a database of magnetic structures. I. The commensurate case. *J. Appl. Crystallogr.* **2016**, *49*, 1750−1776. (b) Gallego, S. V.; Perez-Mato, J. M.; Elcoro, L.; Tasci, E. S.; Hanson, R. M.; Aroyo, M. I.; Madariaga, G. MAGNDATA: towards a database of magnetic structures. II. The incommensurate case. *J. Appl. Crystallogr.* **2016**, *49*, 1941−1956. (c) Perez-Mato, J. M.; Gallego, S. V.; Tasci, E. S.; Elcoro, L.; de la Flor, G.; Aroyo, M. I. Symmetry-Based Computational Tools for Magnetic Crystallography. *Annu. Rev.*

Mater. Res. **2015**, *45*, 217−248 The MAGNDATA database is a free tool, and the reader can access it through the link http://webbdcrista1.ehu.es/magndata/.

(17) (a) Cox, D. E.; Shapiro, S. M.; Cowley, R. A.; Eibschutz, M.; Guggenheim, H. J. *Phys. Rev. B: Condens. Matter Mater. Phys.* **1979**, *19*, 5754−5772. (b) Poole, A.; Roessli, B.; Zaharko, O.; Krämer, K. W. The magnetic structure of multiferroicBaMnF$_4$. *J. Phys.: Condens. Matter* **2011**, *23*, 266004.

(18) Pato-Doldán, B.; Gómez-Aguirre, L. C.; Hansen, P.; Mira, J.; Castro-García, S.; Sánchez-Andújar, M.; Señarís-Rodríguez, M. A.; Zapf, V. S.; Singleton, J. Magnetic transitions and isotropic versus anisotropic magnetic behaviour of $[CH_3NH_3][M(HCOO)_3]$ M = Mn^{2+}, Co^{2+}, Ni^{2+}, Cu^{2+} metal-organic perovskites. *J. Mater. Chem. C* **2016**, *4*, 11164−11172.

(19) Canadillas-Delgado, L.; Mazzuca, L.; Fabelo, O.; Rodríguez-Velamazán, J. A.; Rodríguez-Carvajal, J. Incommensurate structures of the $[CH_3NH_3][Co(COOH)_3]$ compound. *IUCrJ* **2019**, *6*, 105−115.

(20) Rodriguez-Carvajal, J. Recent advances in magnetic structure determination by neutron powder diffraction. *Phys. B* **1993**, *192*, 55−69 The programs of the *FullProf* suite can be obtained at http://www.ill.eu/sites/fullprof.

(21) *JANA2006*: Petricek, V.; Dusek, M.; Palatinus, L. Crystallographic Computing System JANA2006: General features. *Z. Kristallogr. - Cryst. Mater.* **2014**, *229* (5), 345−352.

(22) Ouladdiaf, B.; Archer, J.; Allibon, J. R.; Decarpentrie, P.; Lemée-Cailleau, M.-H.; Rodrıguez-Carvajal, J.; Hewat, A. W.; York, S.; Brau, D.; McIntyre, G. J. CYCLOPS - a reciprocal-space explorer based onCCD neutron detectors. *J. Appl. Crystallogr.* **2011**, *44*, 392−397.

(23) Rodríguez-Carvajal, J.; Fuentes-Montero, L.; Cermak, P. The programs of *ESMERALDA* and their corresponding documentation. https://forge.ill.fr/projects/esmeralda/, 2018

(24) Cañadillas-Delgado, L.; Fabelo, O.; Mazzuca, L.; Rodriguez-Velamazán, J. A.; Rodriguez-Carvajal, J. *Magnetic structure determination of $[CH_3NH_3][M(HCOO)_3]$ ($M = Ni^{2+}$, Cu^{2+}) metal-organic materials*; Institut Laue-Langevin: Grenoble, France, 2019; DOI: 10.5291/ILL-DATA.5-41-947.

(25) Duisenberg, A. J. M. Indexing in single-crystal diffractometry with an obstinate list of reflections. *J. Appl. Crystallogr.* **1992**, *25*, 92−96.

(26) (a) McIntyre, G. J.; Stansfield, R. F. D. A general Lorentz correction for single-crystal diffractometers. *Acta Crystallogr., Sect. A: Found. Crystallogr.* **1988**, *A44*, 257−262. (b) Wilkinson, C.; Khamis, H. W.; Stansfield, R. F. D.; McIntyre, G. J. Integration of single-crystal reflections using area multidetectors. *J. Appl. Crystallogr.* **1988**, *21*, 471−478.

(27) Matthewman, J. C.; Thompson, P.; Brown, P. J. The Cambridge Crystallography Subroutine Library. *J. Appl. Crystallogr.* **1982**, *15*, 167−173.

(28) Sheldrick, G. M. Crystal structure refinement with SHELXL. *Acta Crystallogr., Sect. C: Struct. Chem.* **2015**, *C71*, 3−8.

(29) Palatinus, L.; Chapuis, G. SUPERFLIP - a computer program for the solution of crystal structures by charge flipping in arbitrary dimensions. *J. Appl. Crystallogr.* **2007**, *40*, 786−790.

(30) *Diamond 4.3.1*; Crystal Impact GbR: Bonn, Germany, 2000.

(31) Momma, K.; Izumi, F. VESTA 3 for three-dimensional visualization of crystal, volumetric and morphology data. *J. Appl. Crystallogr.* **2011**, *44*, 1272−1276.

(32) Gomez-Aguirre, L. C.; Pato-Doldán, B.; Mira, J.; Castro-García, S.; Señarís-Rodríguez, M. A.; Sánchez-Andújar, M.; Singleton, J.; Zapf, V. S. Magnetic Ordering-Induced Multiferroic Behavior in [CH3NH3][Co(HCOO)3] Metal-Organic Framework. *J. Am. Chem. Soc.* **2016**, *138*, 1122−1125.

(33) Mazzuca, L.; Canadillas-Delgado, L.; Fabelo, O.; Rodriguez-Velamazan, J. A.; Luzon, J.; Vallcorba, O.; Simonet, V.; Colin, C. V.; Rodriguez-Carvajal, J. Microscopic Insights on the Multiferroic Perovskite-Like $[CH_3NH_3][Co(COOH)_3]$ Compound. *Chem. - Eur. J.* **2018**, *24*, 388−399.

https://dx.doi.org/10.1021/acs.inorgchem.0c01722
Inorg. Chem. XXXX, XXX, XXX−XXX